water

MDPI

Article

Soil Response Induced by Wave Shoaling and Breaking on a Sloping Seabed

Meng-Yu Lin *, Yi-Xiang Lin and Te-Hsing Chang

Department of Civil Engineering, Chung Yuan Christian University, Taoyuan City 320314, Taiwan; ccs99103@gmail.com (Y.-X.L.); tehsing@cycu.edu.tw (T.-H.C.)
* Correspondence: mylin@cycu.edu.tw

Abstract: This study investigates the seabed response induced by wave shoaling and breaking on a sloping seabed through numerical modeling. A coupled approach is employed, integrating a Reynolds-Averaged Navier–Stokes (RANS) wave model with a poro-elastic soil model based on Biot's consolidation theory. The wave model incorporates a stress-ω turbulence model to mitigate the tendency to overestimate turbulence intensity during wave breaking. The numerical simulations capture key hydrodynamic processes such as wave transformation, breaking-induced turbulence, and the evolution of pore pressure and soil stress within the seabed. Model validation against analytical solutions and experimental data confirms the reliability of the numerical framework. The study simulates two types of breaking waves: spilling and plunging breakers. The results indicate that wave breaking significantly alters the spatial and temporal distribution of pore pressures and effective stresses in the seabed. In particular, the undertow generated by breaking waves plays an important role in modulating seabed responses by inducing asymmetric pore pressure and stress distributions. The influence of soil permeability and the degree of saturation on wave-induced responses is investigated, showing that higher permeability facilitates deeper pore pressure penetration, while under lower permeability conditions, a higher degree of saturation significantly enhances pore pressure transmission. Additionally, different breaker types exhibit distinct seabed response characteristics, with plunging breakers causing stronger nonlinear effects. These findings provide valuable insights for the design and stability assessment of marine and coastal infrastructure subjected to dynamic wave loading.

Keywords: wave shoaling; wave breaking; coastal slope; poro-elastic seabed; numerical simulation

check for updates

Academic Editors: Liang Sun and Yu Hu

Received: 25 February 2025
Revised: 23 March 2025
Accepted: 24 March 2025
Published: 27 March 2025

Citation: Lin, M.-Y.; Lin, Y.-X.; Chang, T.-H. Soil Response Induced by Wave Shoaling and Breaking on a Sloping Seabed. *Water* **2025**, *17*, 981. https://doi.org/10.3390/w17070981

Copyright: © 2025 by the authors. Licensee MDPI, Basel, Switzerland. This article is an open access article distributed under the terms and conditions of the Creative Commons Attribution (CC BY) license (https://creativecommons.org/licenses/by/4.0/).

1. Introduction

Surface waves are the primary driving force affecting coastal environments and marine structures. Assessing the interaction between waves and the seabed is crucial for the design and construction of coastal structures such as offshore wind turbines, submarine pipelines, and breakwaters. As waves propagate from the deep ocean to the nearshore, wave transformations such as shoaling, breaking, refraction, diffraction, and reflection occur due to the effects of seabed topography. If waves approach perpendicularly to mildly sloping coasts with alongshore uniform depth contours, wave transformation primarily involves shoaling and breaking. Wave shoaling refers to changes solely caused by shallowing water depth, without altering the propagation direction, leading to reductions in wave celerity and wavelength and an increase in wave steepness. As water depth decreases, waves become steeper and asymmetric due to nonlinear effects, with their crests gradually

tilting forward. This asymmetry increases as waves enter shallower water with higher particle velocities at wave crests, ultimately resulting in crest instability and breaking.

The response of seabed soils to the dynamic pressure generated by periodic waves has been a critical topic of research in coastal engineering. Early theoretical studies primarily focused on the behavior of pore water pressure and soil stress, often assuming constant water depth and neglecting the influence of seabed deformation on wave propagation. These investigations mainly explored how soil properties—such as permeability, elastic modulus, and degree of saturation—affect seabed response, frequently simplifying waves as linear periodic forms, especially in analytical studies. For example, Madsen [1] and Yamamoto et al. [2] provided foundational theoretical models for the response of poroelastic seabeds to water waves based on Biot's consolidation theory [3], laying the groundwork for subsequent developments. Zienkiewicz et al. [4] proposed a simplified version of Biot's consolidation equations known as the u-p approximation, which reduces complexity and minimizes computational demands by neglecting certain acceleration terms. Mei and Foda [5] applied boundary layer theory in their study, simplifying the governing equations within the soil surface region exhibiting a boundary layer profile and conducting an analytical analysis. Okusa [6] simplified the governing equations proposed by Yamamoto et al. [2] into a fourth-order linear differential equation in terms of pore pressure or effective mean normal stress. This approach was used to analyze the soil response of an unsaturated seabed and its phase relationship with the waves. Hsu et al. [7] analyzed the effects of wave obliquity, soil permeability, and stiffness on wave-induced pore pressure, revealing the coupling between wave dynamics and seabed characteristics. Later, Jeng and Cha [8] highlighted the importance of dynamic soil behavior and nonlinear wave effects. Jeng [9] provided a comprehensive review of wave-induced seabed dynamics, discussing both theoretical and practical aspects of wave damping and seabed instability. Ulker et al. [10] compared quasi-static, partially dynamic, and fully dynamic models for saturated seabeds and concluded that wave and soil conditions dictate the most suitable approach. Researchers have also extensively studied seabed liquefaction as a related issue [11,12].

The aforementioned studies primarily focused on soil responses under the influence of waves in uniform water depth. However, as waves propagate into regions of decreasing water depth, the small-amplitude wave assumption becomes inadequate. Instead, the waves undergo complex transformations, including shoaling and eventually breaking, which significantly influence their interaction with the seabed [13–15]. Recent studies have also explored wave–seabed interactions in broader coastal contexts, such as Bragg reflection and harbor resonance mitigation induced by seabed topography. These findings further highlight the relevance of understanding seabed response under varying wave and bathymetric conditions [16–18]. Ting and Kirby [19] conducted laboratory experiments to examine undertow and turbulence in the surf zone, providing foundational data on the impact of breaking waves on sediment transport and seabed behavior. Lin and Liu [20] developed a numerical model to study wave evolution, shoaling, and breaking in the surf zone, utilizing the Reynolds equations for mean flow and the k-ϵ turbulence model to analyze turbulent kinetic energy and dissipation. Dong et al. [21] and Ma et al. [22] demonstrated that nonlinear wave parameters, such as skewness and asymmetry, are significantly affected by the slope of the seabed. Zhang and Benoit [23] further explored the effects of steep seabed changes on the occurrence of extreme waves, highlighting the role of wave-seabed interaction in coastal hazards. Larsen and Fuhrman [24] and Li et al. [25] investigated turbulence modeling for breaking surface waves. Instability was identified in the Reynolds-Averaged Navier–Stokes (RANS) models with common two-equation turbulence closures, such as k-ω and k-ϵ, which leads to unphysical turbulence growth

in pre-breaking regions [24]. In contrast, the stress-ω model was shown to be neutrally stable, preventing turbulence overproduction and providing more accurate predictions of undertow velocity profiles in surf zone breaking waves [25]. Rafiei et al. [26] investigated wave-induced responses and instability of sloping seabeds using a coupled finite element model that considers interactions between fluid motion and porous seabeds. However, their study did not include the nonlinear effects of waves and the turbulent effects of wave breaking.

From the literature review, it is evident that while wave transformations over sloping seabeds have been extensively studied, research on the resulting seabed soil responses remains relatively limited, especially under breaking wave conditions. To address this gap, this study employs a numerical model based on the finite volume method (FVM) that integrates the RANS wave model with a poroelastic seabed model. We selected the RANS model for its capability to capture wave shoaling and breaking, and employed the stress-ω turbulence closure to improve turbulence predictions. The stress-ω model has been shown to avoid overproduction of turbulence prior to wave breaking and yield more accurate undertow predictions, particularly in the inner surf zone where other models (e.g., k-ϵ, k-ω) tend to overestimate flow velocities [24,25]. The poroelastic seabed model, based on Biot's consolidation theory, effectively characterizes the evolution of pore pressure and effective stress in response to wave-induced loading. This approach accounts for both the solid deformation and fluid flow within the seabed, providing a more comprehensive representation of soil behavior under dynamic wave loading. Unlike purely elastic or static models, Biot's theory enables the prediction of transient pore pressure changes and soil settlement, which are critical for assessing seabed stability in coastal engineering applications. Building upon and extending previous numerical studies, this research aims to investigate seabed responses to wave shoaling and breaking, emphasizing the effects of turbulence and soil properties.

2. Mathematical Models

This study utilizes the finite volume method (FVM) to numerically simulate two-dimensional wave shoaling and breaking over a sloping seabed and its corresponding impact on the seabed soil response. The numerical framework consists of two components:

1. Wave Model: A Reynolds-Averaged Navier–Stokes (RANS)-based hydrodynamic model that captures wave transformation, breaking, and turbulence effects. The model incorporates the stress-ω turbulence closure [27], which enhances stability and accuracy in predicting turbulence intensity throughout the breaking process. Unlike traditional k-ω and k-ϵ models, the stress-ω model mitigates the overproduction of turbulence in the pre-breaking region and provides improved undertow velocity predictions in surf zones.
2. Seabed Model: A poroelastic soil model based on Biot's consolidation theory, which evaluates the wave-induced pore pressure and effective stress distribution within the seabed.

We establish the interaction between the two models through a one-way coupling approach [28], where we first compute wave-induced dynamic pressures at the seabed and then apply them as boundary conditions in the seabed model. This approach assumes that seabed deformation and fluid exchange within the soil do not significantly influence the wave field, ensuring computational efficiency while maintaining accuracy in predicting seabed responses. The following subsections detail the governing equations for both the wave and soil models.

2.1. Wave Model

2.1.1. RANS Equations

In the wave model, the flow of both air and water is assumed to be incompressible turbulent flow. The two-phase flow field induced by wave transformation and breaking is simulated using the RANS equations coupled with the stress-ω turbulent model proposed by Wilcox (2006) [27]. The continuity and momentum equations, describing the motion of fluids under turbulent conditions, are formulated using index notation as

$$\frac{\partial u_i}{\partial x_i} = 0, \tag{1}$$

$$\frac{\partial u_i}{\partial t} + u_j \frac{\partial u_i}{\partial x_j} = -\frac{1}{\rho_f}\frac{\partial p_d}{\partial x_i} + \frac{\partial}{\partial x_j}\left(2\nu S_{ji} - \overline{u_j' u_i'}\right), \tag{2}$$

where x_i are the Cartesian coordinates, u_i are the mean (Reynolds-averaged) components of the fluid velocity, ρ_f is the fluid density, which can represent the air density ρ_a or the water density ρ_w, ν is the kinematic fluid viscosity, and t is time. p_d denotes the dynamic wave pressure defined as $p_d = p - \rho_f g_j x_j$, where p is the total pressure and g_j is the gravitational acceleration vector. The strain-rate tensor S_{ij} is given by

$$S_{ij} = \frac{1}{2}\left(\frac{\partial u_i}{\partial x_j} + \frac{\partial u_j}{\partial x_i}\right), \tag{3}$$

and the Reynolds stress tensor induced by the turbulent fluctuation velocity u_i' is defined as

$$\tau_{ij} = -\overline{u_i' u_j'} \tag{4}$$

with the overbar denoting Reynolds averaging.

To track the free surface between air and water, the volume of fluid (VOF) method [29] is employed. The volume fraction function F is governed by:

$$\frac{\partial F}{\partial t} + \frac{\partial (u_i F)}{\partial x_i} + \frac{\partial [u_{ri}(1-F)F]}{\partial x_i} = 0, \tag{5}$$

where u_{ri} is a relative velocity [30]; $F = 1$ represents water, $F = 0$ represents air, and $0 < F < 1$ corresponds to the interface region.

2.1.2. Turbulence Closure Model

The stress-ω model [27] employed for the turbulent closure consists of the following transport equations for the Reynolds stress τ_{ij} and the specific rate of dissipation ω as [25]

$$\frac{\partial \bar{\rho}_f \tau_{ij}}{\partial t} + \bar{u}_k \frac{\partial \bar{\rho}_f \tau_{ij}}{\partial x_k} = -\bar{\rho}_f P_{ij} + \frac{2}{3}\bar{\rho}_f \beta^* \omega k_t \delta_{ij} - \bar{\rho}_f \Pi_{ij} + \bar{\rho}_f \alpha_b^* \frac{k_t}{\omega} N_{ij} + \frac{\partial}{\partial x_k}\left[\bar{\rho}_f \left(\nu + \sigma^* \frac{k_t}{\omega}\right)\frac{\partial \tau_{ij}}{\partial x_k}\right], \tag{6}$$

$$\frac{\partial \bar{\rho}_f \omega}{\partial t} + \bar{u}_j \frac{\partial \bar{\rho}_f \omega}{\partial x_j} = \bar{\rho}_f \alpha \frac{\omega}{k_t}\tau_{ij}\frac{\partial \bar{u}_i}{\partial x_j} - \bar{\rho}_f \beta \omega^2 + \sigma_d \frac{\bar{\rho}_f}{\omega}\frac{\partial k_t}{\partial x_j}\frac{\partial \omega}{\partial x_j} + \frac{\partial}{\partial x_k}\left[\bar{\rho}_f \left(\nu + \sigma \frac{k_t}{\omega}\right)\frac{\partial \omega}{\partial x_k}\right]. \tag{7}$$

In the above equations, δ_{ij} is Kronecker delta, $\bar{\rho}_f$ is the Reynolds-averaged fluid density, and k_t is the turbulent kinetic energy (per unit mass) given by

$$k_t = -\frac{1}{2}\tau_{kk}. \tag{8}$$

The Brunt-Väisälä frequency tensor N_{ij} for describing the buoyancy-induced turbulence is

$$N_{ij} = \frac{1}{\rho_0}\left(g_i\frac{\partial\bar{\rho}_f}{\partial x_j} + g_j\frac{\partial\bar{\rho}_f}{\partial x_i}\right), \tag{9}$$

where ρ_0 is the reference density of the fluid. The pressure–strain correlation has the form:

$$\Pi_{ij} = \beta^* C_1\omega\left(\tau_{ij} + \frac{2}{3}k_t\delta_{ij}\right) - \hat{\alpha}\left(P_{ij} - \frac{2}{3}P\delta_{ij}\right) - \hat{\beta}\left(D_{ij} - \frac{2}{3}P\delta_{ij}\right) - \hat{\gamma}k_t\left(S_{ij} - \frac{1}{3}S_{kk}\delta_{ij}\right), \tag{10}$$

where

$$P_{ij} = \tau_{im}\frac{\partial u_j}{\partial x_m} + \tau_{jm}\frac{\partial u_i}{\partial x_m}, \tag{11}$$

$$D_{ij} = \tau_{im}\frac{\partial u_m}{\partial x_j} + \tau_{jm}\frac{\partial u_m}{\partial x_i}, \tag{12}$$

$$P = \frac{1}{2}P_{kk}. \tag{13}$$

The closure coefficients are [25,27]

$$C_1 = 9/5, \quad C_2 = 10/19, \quad \hat{\alpha} = (8 + C_2)/11, \quad \hat{\beta} = (8C_2 - 2)/11, \quad \hat{\gamma} = (60C_2 - 4)/55,$$
$$\alpha = 13/25, \quad \alpha_b^* = 1.36, \quad \beta_0 = 0.0708, \quad \beta^* = 9/100, \quad \beta = \beta_0 f_\beta, \quad \sigma = 0.5, \quad \sigma^* = 0.6,$$
$$\sigma_d = \begin{cases} 0, & \frac{\partial k_t}{\partial x_j}\frac{\partial\omega}{\partial x_j} \le 0 \\ 1/8, & \frac{\partial k_t}{\partial x_j}\frac{\partial\omega}{\partial x_j} > 0, \end{cases}$$

and

$$f_\beta = \frac{1 + 85\chi_\omega}{1 + 100\chi_\omega}, \quad \chi_\omega = \left|\frac{\Omega_{ij}\Omega_{jk}\hat{S}_{ki}}{(\beta^*\omega)^3}\right|, \quad \hat{S}_{ki} = S_{ki} - \frac{1}{2}\frac{\partial u_m}{\partial x_m}\delta_{ki}, \quad \Omega_{ij} = \frac{1}{2}\left(\frac{\partial u_i}{\partial x_j} - \frac{\partial u_j}{\partial x_i}\right).$$

2.2. Soil Model

The seabed soil is considered a multi-phase, a nearly saturated poroelastic medium consisting of soil particles, water, and air. For the soil skeleton, the effective stress is defined by

$$\sigma'_{ij} = \sigma_{ij} + p\delta_{ij}, \tag{14}$$

where σ_{ij} and σ'_{ij} are the total and effective stress tensors of soil, respectively, and p is the pore fluid pressure. The stress–strain relation for the isotropic soil materials by Hooke's law is expressed as

$$\sigma'_{ij} = \left(K - \frac{2}{3}G\right)\epsilon\delta_{ij} + 2G\epsilon_{ij}, \tag{15}$$

where $\epsilon_{ij} = \frac{1}{2}\left(\frac{\partial U_i}{\partial x_j} + \frac{\partial U_j}{\partial x_i}\right)$ is the strain tensor, U_j is the j-th component of the displacement vector, $\epsilon = \epsilon_{kk} = \frac{\partial U_k}{\partial x_k}$ is the volumetric strain, $K = \frac{E}{3(1-2\mu)}$ is the bulk modulus, $G = \frac{E}{2(1+\mu)}$ is the shear modulus, E is Young's modulus, and μ is Poisson's ratio.

The dynamic response of seabed soil under wave loading is governed by the partial dynamic u-p approximation [4] of Biot's consolidation theory [3], in which the displacements of the pore fluid relative to soil particles are neglected, but the accelerations of the pore fluid and soil particles are included. The equations for the force equilibrium in (nearly) saturated soil are

$$G\left(\frac{\partial^2 U_i}{\partial x_j\partial x_j} + \frac{1}{1-2\mu}\frac{\partial\epsilon}{\partial x_i}\right) = \frac{\partial p}{\partial x_i} - \rho\frac{\partial^2 U_i}{\partial t^2}, \tag{16}$$

where ρ denotes the total density of seabed sediment defined as

$$\rho = n\rho_f + (1-n)\rho_s \tag{17}$$

with n as the soil porosity and ρ_s as the soil density. The continuity equation of the pore fluid flow based on Darcy's law with isotropic permeability is

$$\frac{n}{K'}\frac{\partial p}{\partial t} - \frac{k}{\rho_f g}\frac{\partial^2 p}{\partial x_j \partial x_j} + \frac{\partial \epsilon}{\partial t} + \frac{k}{g}\frac{\partial}{\partial x_j}\left(\frac{\partial^2 U_j}{\partial t^2}\right) = 0, \tag{18}$$

where k denotes the permeability of the soil. The bulk modulus of the compressible pore fluid K' is approximated as

$$\frac{1}{K'} = \frac{1}{K_w} + \frac{1-S_r}{p_{w_0}}, \tag{19}$$

where K_w is the bulk modulus of pure water (generally taken as 2×10^9 N/m^2), S_r is the degree of soil saturation, and p_{w_0} is the absolute pore water pressure at the seabed.

3. Numerical Approach

3.1. Numerical Models

In this study, we perform the numerical modeling of the wave-induced flow field and the resulting soil response using the finite volume method (FVM). We employ the open-source CFD tool OpenFOAM as the modeling platform. Based on the differences in the fundamental equations, we divide the numerical modeling into two parts: the wave model and the soil model, and we link them using the one-way coupling approach introduced in Section 2.

The main functions required for the wave model include incorporating wave generation and absorption boundary conditions, simulating the wave-induced flow field as a two-phase flow, and tracking the free surface position using the VOF method. In the present work, we use the waves2Foam toolbox [31] to model wave generation and absorption, and we apply the Wilcox (2006) turbulence model [25,27] to address the turbulence effects associated with wave shoaling and breaking.

Assuming that the seabed soil response does not affect the wave-induced flow field, we first simulate the nonlinear wave shoaling and breaking on the sloping seabed. Then, we apply the one-way coupling approach, using the dynamic pressure generated by the surface waves as the boundary condition for the soil model. We use the upFoam toolbox [28], which is based on Biot's theory and employs the partial dynamic *u-p* approximation.

3.2. Computational Domain and Boundary Conditions

Figure 1 shows the schematic diagram of the computational domain and the boundary conditions. For comparison purposes, the computational domain setup is similar to the breaking wave experiments by [19] and the numerical study by [25]. In the wave model, the stream-function wave theory is employed as the wave generation boundary condition to generate nonlinear waves. A relaxation zone with a length of one wavelength is set at the left side to eliminate spurious reflections from the boundary. During the wave model calculations, the seabed is assumed to be rigid with a no-slip boundary condition, meaning the pressure has a zero normal gradient, the flow velocity is zero, and the soil skeleton has zero displacement.

In the soil model, at the wave-seabed interface, the soil traction T_i is zero. The traction is defined as $T_i = \sigma_{ij} n_j$ with being n_j the surface normal vector. The excess pore-fluid pressure at the interface is equal to the dynamic pressure of the waves on the seabed, as provided by the wave model. At the lateral boundaries of the soil model, the pore pressure

has a zero normal gradient, and sliding displacement of the soil skeleton is allowed. At the bottom of the soil, the normal gradient of the pore pressure and the displacement of the soil skeleton are both zero.

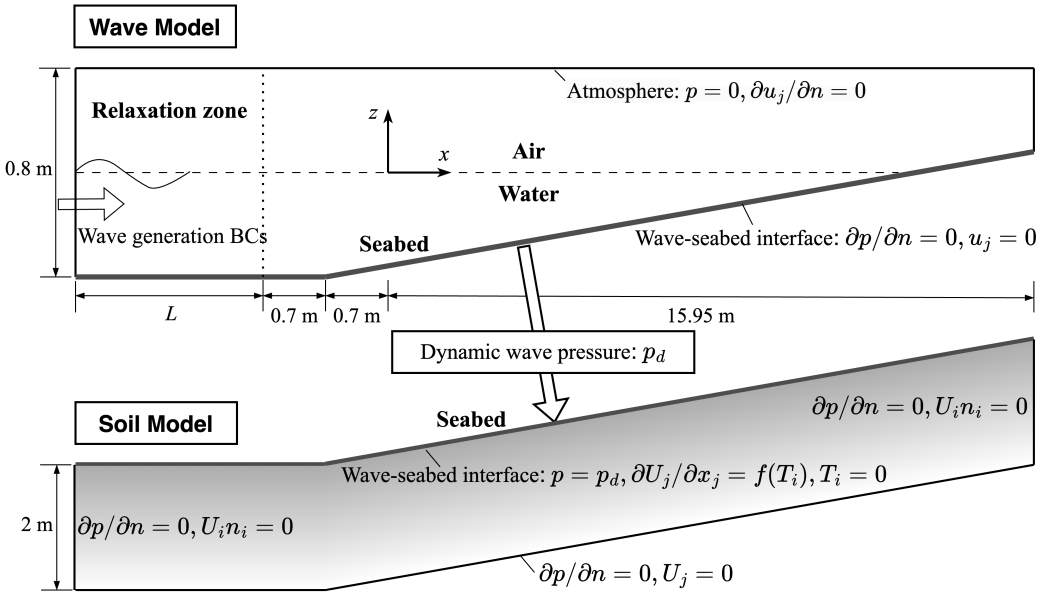

Figure 1. Schematic diagram of the computational domain and the boundary conditions (the dimensions are not to scale).

4. Model Verification

The model validation was conducted in two steps. First, under linear wave conditions over a flat seabed, the wave model was validated against analytical solutions for free surface elevation and dynamic pressure, while the seabed model was validated using analytical solutions for pore pressure and stress distribution under various soil properties. Then, for wave shoaling and breaking over a sloping seabed, the accuracy of the wave model is further examined through comparisons of free surface envelopes with the experimental results of Ting and Kirby [19], which are presented in Section 5.

4.1. Wave Model

Applying the small amplitude wave theory, for a linear periodic wave propagating in a constant water depth, the surface elevation and the dynamic wave pressure are given by:

$$\eta = \frac{H}{2}\cos(k_f x - \omega_f t), \tag{20}$$

and

$$p_d = \frac{\rho_f g H}{2}\frac{\cosh k_f(h+z)}{\cosh k_f h}\cos(k_f x - \omega_f t), \tag{21}$$

where η is the free-surface elevation relative to the still water level, p_d is the dynamic wave pressure at the seabed, H is the wave height, h is the still water depth, $k_f = 2\pi/L$ is the wave number with L the wave length, and $\omega_f = 2\pi/T$ is the angular frequency with T the period of waves.

The modeled wave conditions are listed in Table 1. The computational domain has a length of 48 m, approximately 7.7 wavelengths. Relaxation zones, each one wavelength long, are placed at both the left and right lateral boundaries to absorb reflected waves. The mesh size is set to $\Delta x = 0.1$ m, $\Delta z = 0.01$ m. Figure 2 presents the computed time variations in free-surface elevation over three periods, along with a comparison to the analytical solution. Figure 3 compares the numerical and analytical results for the vertical

distribution of dynamic wave pressure at different times ($t = 0T, 0.3T, 0.5T, 0.8T$) within a single period. These comparisons demonstrate good agreement.

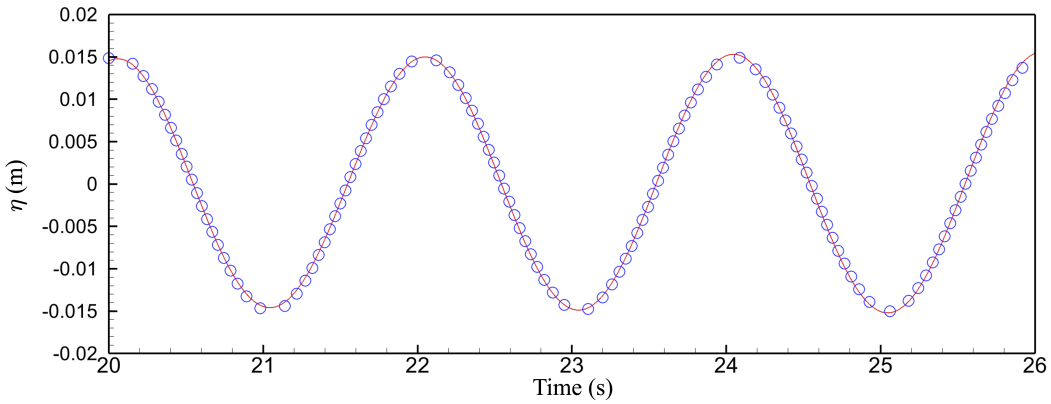

Figure 2. Comparison of the computed free surface elevation of linear waves (——) with the analytical solution (○).

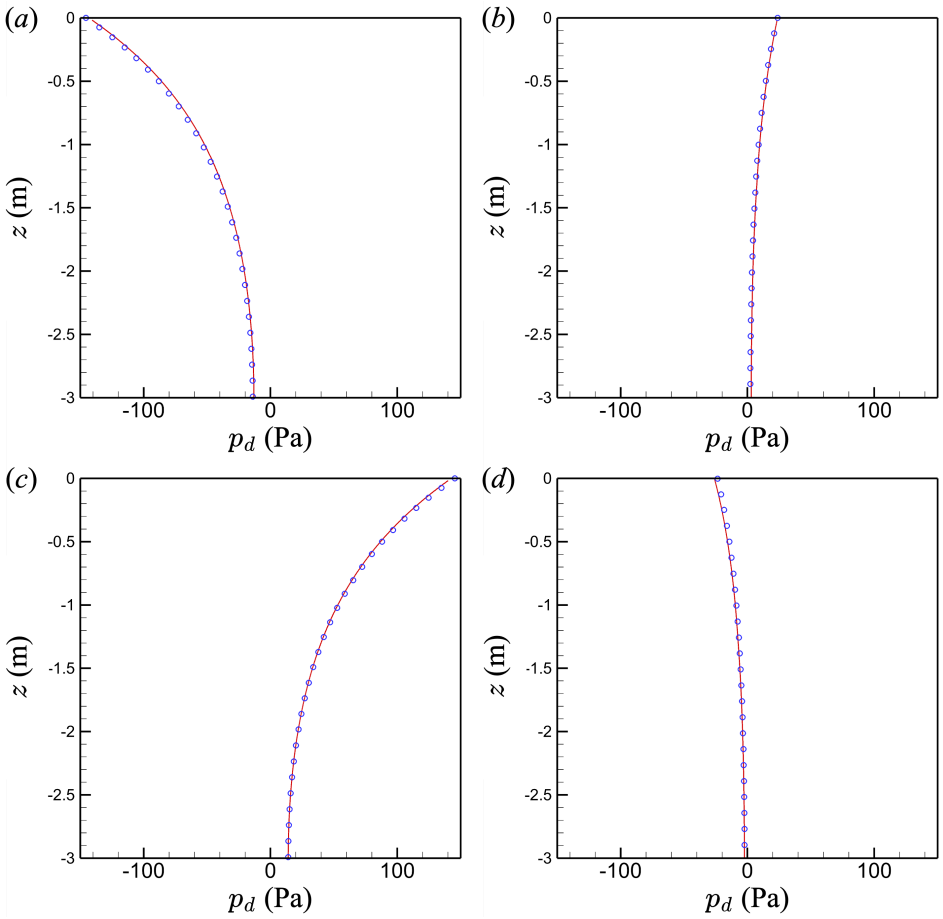

Figure 3. Comparisons of the computed dynamic wave pressure of linear waves (——) with the analytical solution (○) at (**a**) $t = 0T$, (**b**) $t = 0.3T$, (**c**) $t = 0.5T$ and (**d**) $t = 0.8T$.

Table 1. Wave conditions for linear-wave validation case.

Parameter	Description	Value
H (m)	Wave height	0.03
h (m)	Water depth	3.0
L (m)	Wave length	6.21
T (s)	Wave period	2.0

4.2. Soil Model

For the validation of the soil model, the seabed thickness is set to 3 m and the length to 48 m. The soil parameters are based on the model validation case from Rafiei et al. [26] in their numerical study, as shown in Table 2. After considering the results of the convergence test for grid resolution, the mesh size is set to $\Delta x = 1$ m and $\Delta z = 0.01$ m. The calculated dynamic wave pressure on the seabed from linear waves, as described in the previous subsection, is used as the upper boundary condition in the soil model to compute the induced soil response.

Table 2. Soil conditions for linear-wave validation case.

Parameter	Description	Value
d (m)	Soil depth	3.0
k (m/s)	Permeability	0.0001
S_r (m)	Degree of soil saturation	0.95
G (Pa)	Shear modulus	10^7
E (Pa)	Young's modulus	2.6×10^7
K (Pa)	Bulk modulus	2×10^9
ρ_s (kg/m^3)	Soil density	1720
ρ_f (kg/m^3)	Water density	1000
n	Porosity	0.35
μ	Poisson's ratio	0.3

Hsu and Jeng [32] proposed an analytical solution for the wave-induced soil response in an unsaturated, anisotropic seabed of finite thickness. The analytical solution is employed to validate the soil model. Figure 4 shows the computed vertical distribution of maximum effective stress and pore water pressure induced by linear waves, compared with the analytical solution [32]. In the figure, p_0 represents the amplitude of the dynamic pressure at the seabed. The comparison reveals that the numerical results for pore water pressure and each stress component are in good overall agreement with the analytical solution, indicating that the model accurately simulates the soil response induced by water waves.

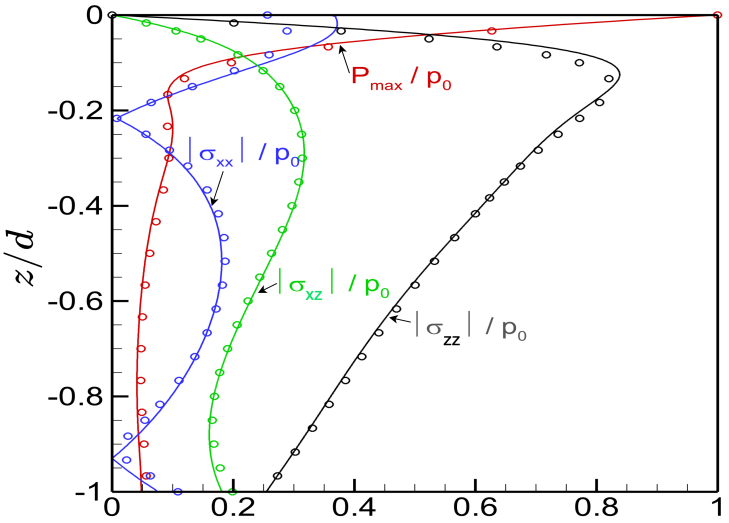

Figure 4. Comparison of the computed soil response (——) with the analytical solution [32] (○).

Since the analytical solution [32] is based on a quasi-static model that neglects the accelerations due to fluid and soil motion, differing from the partial dynamic model of this numerical approach, their results may not be completely consistent. To investigate this phenomenon, cases with different depth-to-wavelength ratios, permeability, and degree of saturation of soil were tested. The conditions for these cases are listed in Table 3, and the comparison between the numerical results and the analytical solution for the maximum pore water pressure of each case is shown in Figure 5. The comparisons reveal that for greater soil depths (comparable in magnitude to the wavelength, as in Cases V.1 to V.3), the numerical results are consistent with the analytical solution and remain unaffected by soil permeability and saturation degree. However, when the soil depth is relatively shallow compared to the wavelength and the permeability is relatively small (Cases V.4 and V.5), the differences between the numerical results and the analytical solution become more noticeable.

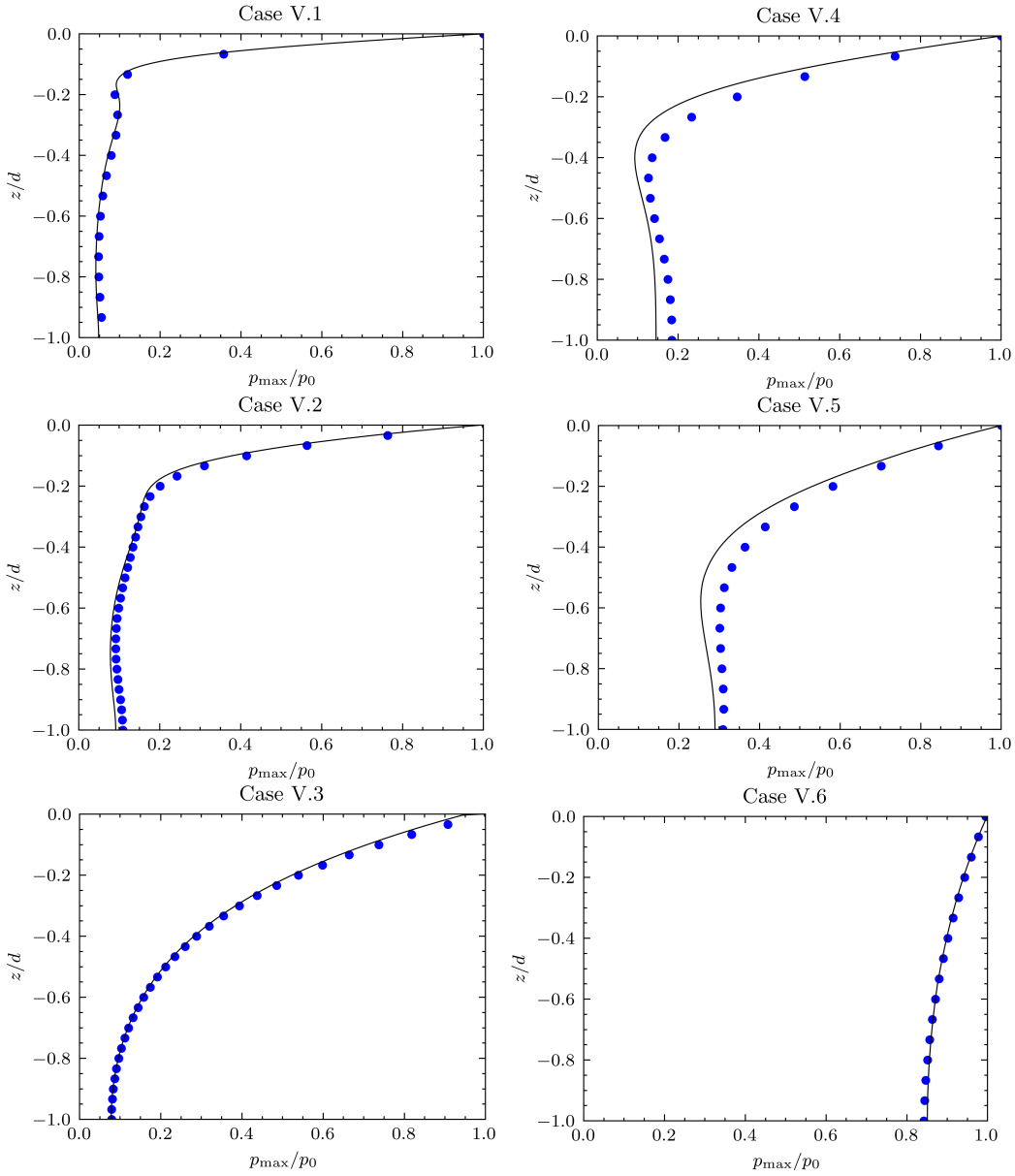

Figure 5. Comparison of the numerical results (——) and the analytical solution [32] (○) for maximum pore pressure under different conditions.

Table 3. The conditions for the cases comparing the numerical results with the analytical solution.

Case No.	d (m)	L (m)	d/L	k (m/s)	S_r
V.1	3.0	6.21	0.483	0.0001	0.95
V.2	3.0	6.21	0.483	0.0001	0.98
V.3	3.0	6.21	0.483	0.01	0.95
V.4	1.5	18.96	0.08	0.0001	0.95
V.5	1.5	18.96	0.08	0.0001	0.98
V.6	1.5	18.96	0.08	0.01	0.95

5. Results and Discussion

To examine the soil response induced by wave shoaling and breaking, we adopt wave conditions from the laboratory experiments of Ting and Kirby [19] for spilling and plunging breakers. We consider two different wave conditions: a spilling breaker with a period of 2.0 s and a plunging breaker with a period of 5.0 s. In both cases, the wave height in the uniform-depth region is approximately 0.13 m. Table 4 summarizes the wave parameters and the measured breaking point x_b. Regarding the seabed properties, we use the same soil parameters as in the validation case (Table 2), except for permeability, saturation, and depth. To examine the effects of permeability and saturation on the seabed response, we define four simulation conditions, as shown in Table 5. These soil parameters represent typical values for medium-dense sandy seabeds, based on values reported in the literature [26]. While the current study focuses on the influence of permeability and saturation, other properties, such as Young's modulus and porosity, may also influence the seabed response.

Table 4. Wave conditions for the breaking wave cases.

Breaker Type	H (m)	T (s)	L (m)	$K_f H$	$k_f h$	x_b (m)
Spilling	0.125	2.0	3.69	0.208	0.664	6.400
Plunging	0.128	5.0	9.79	0.076	0.238	7.795

Table 5. Soil permeability and saturation conditions of the sloping seabed.

Case No.	k (m/s)	S_r
1	0.0001	0.95
2	0.01	0.95
3	0.0001	0.98
4	0.01	0.98

The computational domain is shown in Figure 1, where the horizontal length of the sloped section is 16.65 m with a slope of 1:35. The length of the flat section is approximately 5 m, with a still water depth of 0.4 m. The depth of the soil region is 2 m. The grid size of the wave model domain, based on [24], is set to $\Delta x = \Delta z = 0.01$ m in the flat section, and $\Delta x \simeq \Delta z \simeq 0.0063$ m in the sloped section. The vertical grid near the seabed is refined to $\Delta z u_\tau / \nu < 30$ to ensure proper simulation of the turbulent viscous sublayer, with u_τ being the friction velocity. For the soil model, the grid size is $\Delta x = 0.1$ m and $\Delta z = 0.01$ m.

5.1. Spilling Breaker

Figure 6 shows the comparison of the computed water surface elevation envelope of the spilling breaker simulation with the experimental measurement [19], where $\langle \eta \rangle$ represents the period-averaged water level, and $\eta_{\max}$ and $\eta_{\min}$ denote the maximum and minimum water levels, respectively. The comparison reveals that the model can reasonably capture the wave shoaling and breaking phenomena, including the trend of wave height

variation and the location of the breaking point. The five points x_1 to x_5 shown in Figure 6 represent the output locations for the computational results discussed later. Among them, x_1 ($x = -2$ m) is in the uniform-depth section, x_2 ($x = 2$ m) and x_3 ($x = 5$ m) are in the shoaling region on the slope, while x_4 ($x = 7$ m) and x_5 ($x = 10$ m) are in the breaking region. Figure 7 displays the computed free-surface elevation at the five locations during the time interval $t = 75T \sim 78T$. The points in the figure represent the output times within a period (t_1 to t_5), corresponding to the vertical distribution of pore pressure and soil stresses at each location (see Figures 9–12). Figure 7 illustrates that as the waves enter the sloping section, the nonlinear effects caused by shoaling gradually increase the wave height, reaching its peak just before breaking. The breaking of waves leads to a significant decrease in wave height, releasing wave energy into the water, which generates notable turbulence and induces an undertow.

Figure 8 presents instantaneous excess pore water pressure contours in the seabed soil under the action of the spilling breaker for different permeability conditions (Case 1: $k = 0.0001$ m/s, Case 2: $k = 0.01$ m/s). The portion above the seabed displays the horizontal velocity component of the water and air. Before wave breaking, due to the dynamic pressure of periodic waves, the excess pore water pressure in the seabed soil exhibits a periodic spatial distribution along the wave propagation direction. After wave breaking, as the periodic wave action diminishes and an offshore-directed undertow forms, the excess pore water pressure predominantly displays positive values. The extension of excess pore water pressure into the deeper depths of the soil exhibits a slightly inclined distribution due to the transmission of stress, and it extends deeper in the soil with higher permeability.

To understand the temporal variations of pore-water pressure and stress components before and after wave breaking, the results for output points x_3 (before breaking) and x_5 (after breaking) in Case 1 are shown in Figures 9 and 10, respectively. Similarly, the results for these two points in Case 2 are presented in Figures 11 and 12. In these figures, t_1 to t_5 represent instantaneous times spaced one quarter wave period apart from one wave crest to the next, as presented in Figure 7. First, the differences in soil response before and after the breaking point are compared. At x_3, the free-surface profile exhibits higher crests and milder troughs due to the nonlinear effect caused by shoaling, resulting in an asymmetric cyclic soil response. As shown in Figures 9 and 11, p reaches higher values at the wave crest ($t = t_1$) compared to the wave trough ($t = t_3$), while σ_{zz} follows an opposite trend. At x_5, located after the breaking point, the free-surface fluctuations are relatively subdued, while the turbulent effects of the breaking wave generate an offshore-directed undertow. As a result, p exhibits small-amplitude periodic oscillations with a positive net value, while σ_{xz} and σ_{zz} show oscillations with negative net values. The net shift in σ_{xx} is less pronounced.

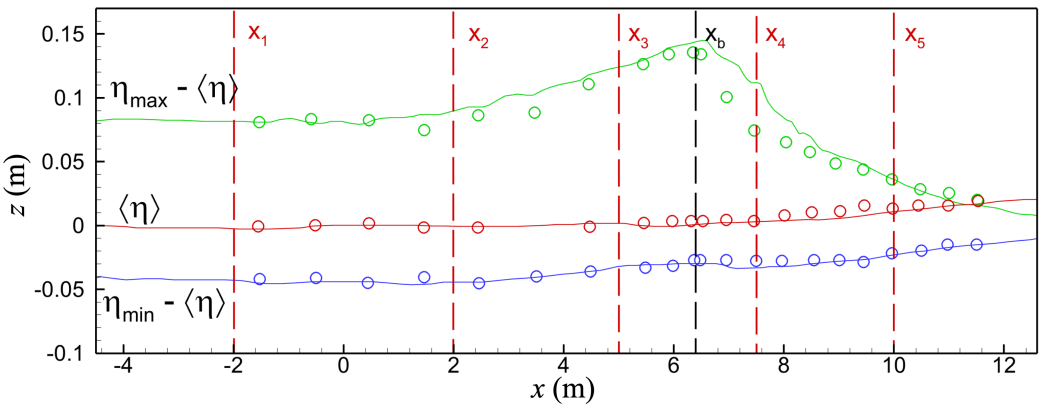

Figure 6. Period-averaged surface elevation envelopes (——) for the spilling breaker simulation, comparing with the experimental measurement [19] (○).

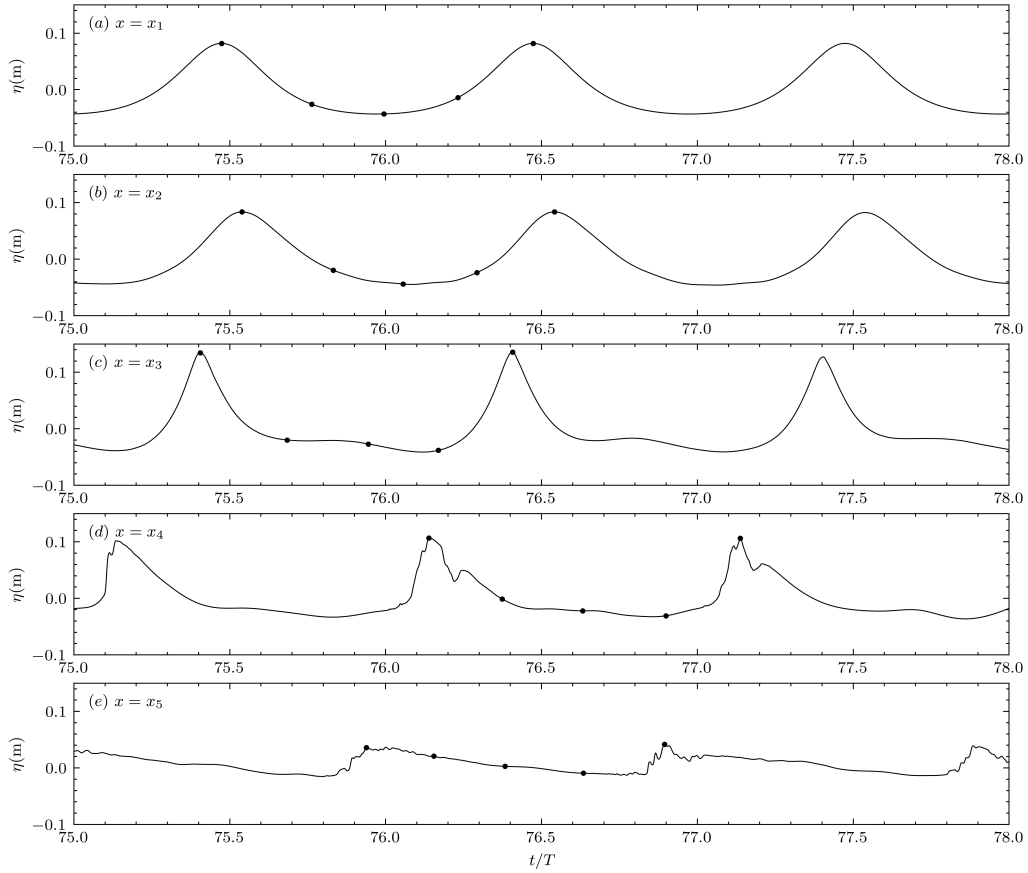

Figure 7. Time variation of free-surface elevation at different locations in the spilling breaker simulations. Points indicate the output times (t_1 to t_5), corresponding to the vertical distribution of pore pressure and soil stresses at each position.

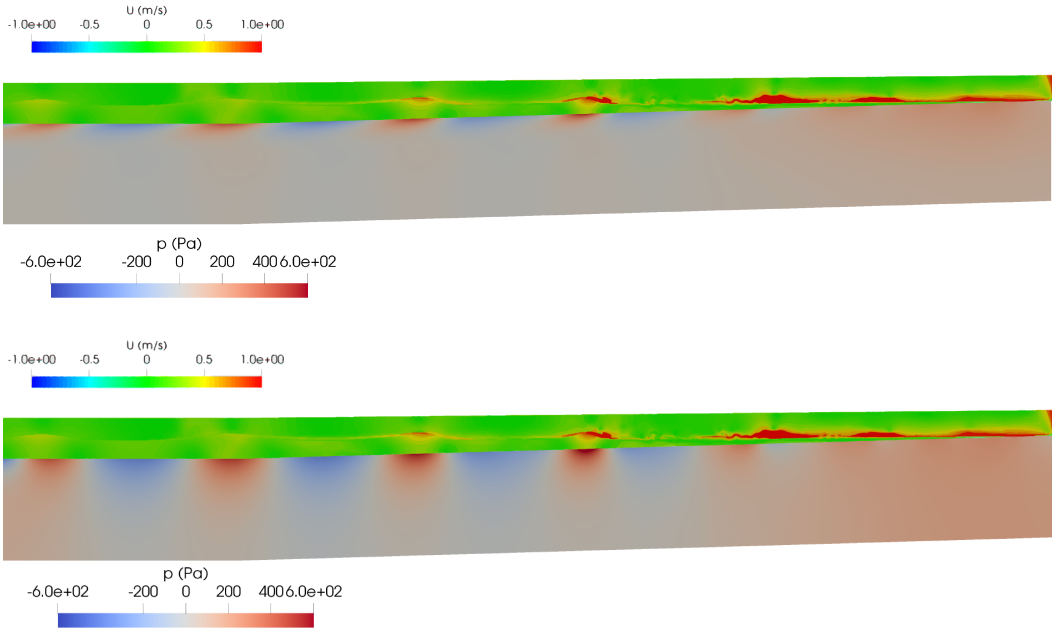

Figure 8. Horizontal fluid velocity and pore pressure contours for Case 1 ($k = 0.0001$ m/s, upper panel) and Case 2 ($k = 0.01$ m/s, lower panel) of spilling breaker simulations.

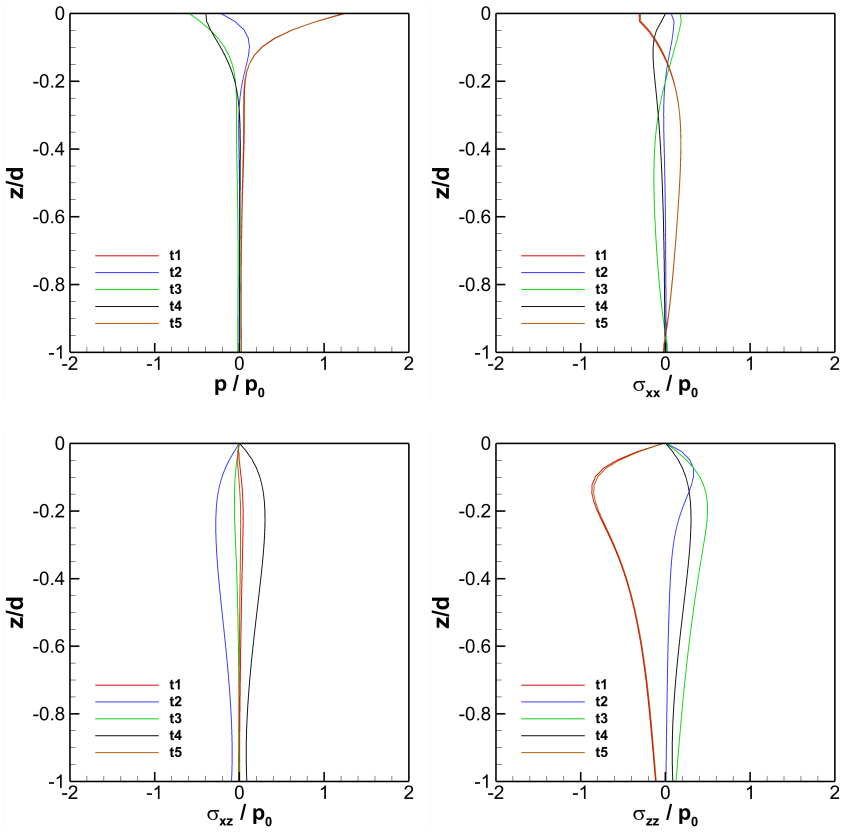

Figure 9. Time variation of pore pressure and soil stresses at location x_3 over one wave period for Case 1 ($k = 0.0001$ m/s) of the spilling breaker simulations.

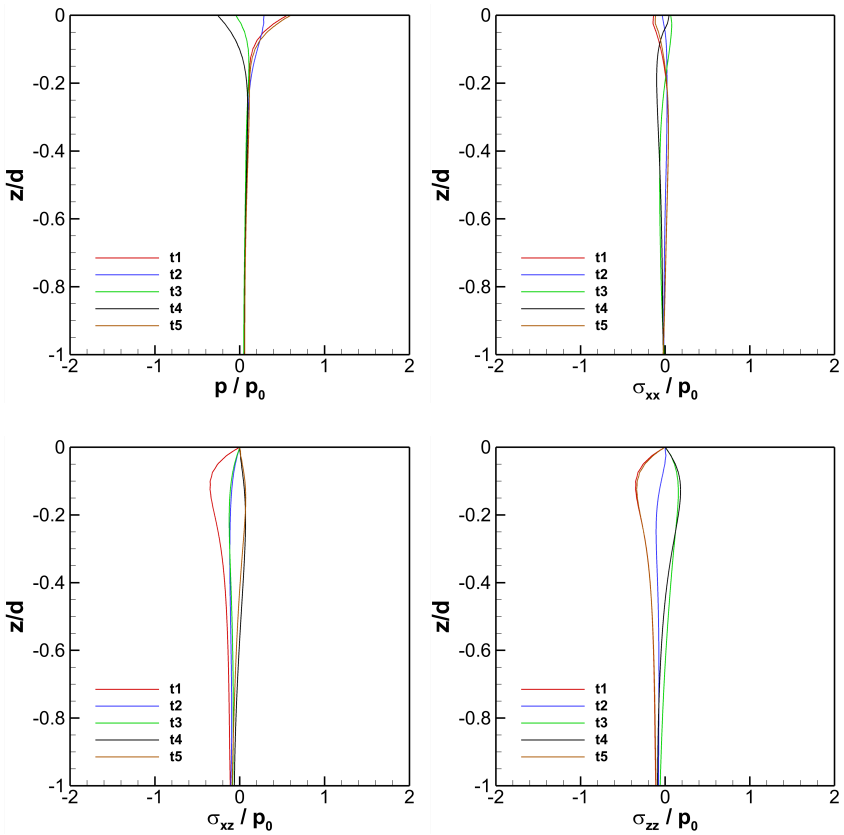

Figure 10. Time variation of pore pressure and soil stresses at location x_5 over one wave period for Case 1 ($k = 0.0001$ m/s) of the spilling breaker simulations.

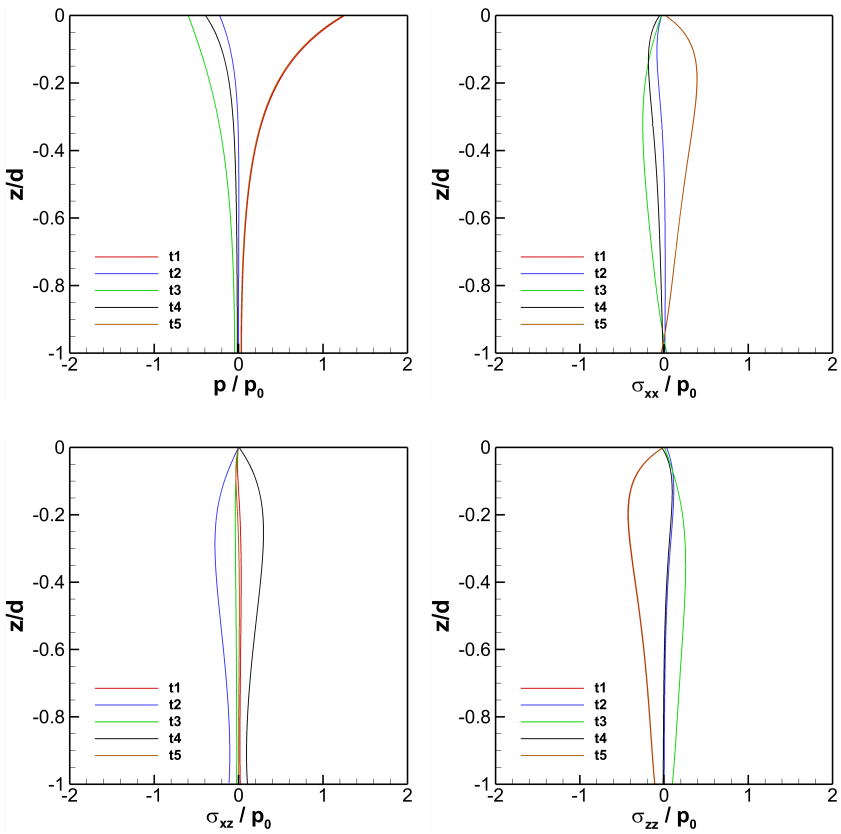

Figure 11. Time variation of pore pressure and soil stresses at location x_3 over one wave period for Case 2 ($k = 0.01$ m/s) of the spilling breaker simulations.

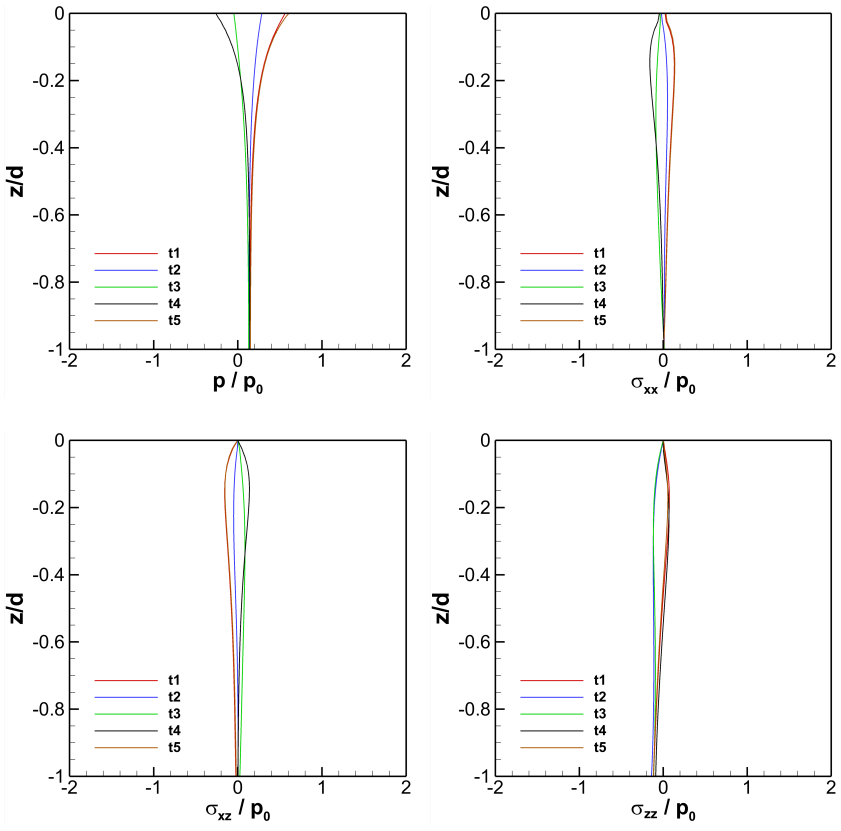

Figure 12. Time variation of pore pressure and soil stresses at location x_5 over one wave period for Case 2 ($k = 0.01$ m/s) of the spilling breaker simulations.

Next, the impact of soil permeability on pore water pressure and stress is examined. Overall, when permeability is higher, pore water pressure transmits to greater soil depths, and the delay in cyclic oscillations along the depth direction is less pronounced. Conversely, when permeability is lower, pore water pressure oscillations are confined to a shallower soil depth, with a more noticeable delay in the depth direction. The distribution trend of σ_{xx} influenced by permeability is similar to that of p. In contrast, σ_{xz} is less affected by permeability. The trend of σ_{zz} is somewhat different regarding permeability. When the k value is smaller, due to the shallower transmission of pore water pressure, larger extreme values (both positive and negative) of σ_{zz} appear between $-0.1 \geq z/d \geq -0.2$. Conversely, when the k value is larger, the transmission area of pore water pressure extends deeper, resulting in much smaller extreme values of σ_{zz}.

Figure 13 presents the distribution of excess pore pressure at different locations along the slope under various soil permeability and saturation conditions at the wave crest ($t = t_1$). This figure highlights the combined effects of permeability and saturation degree on pore pressure within the seabed. The results indicate that higher permeability allows pore pressure to propagate deeper into the soil. When the permeability is relatively high, the effect of saturation degree is less pronounced. However, at lower permeability values, the degree of saturation has a more significant influence, with increasing saturation degree leading to higher pore pressure within the seabed.

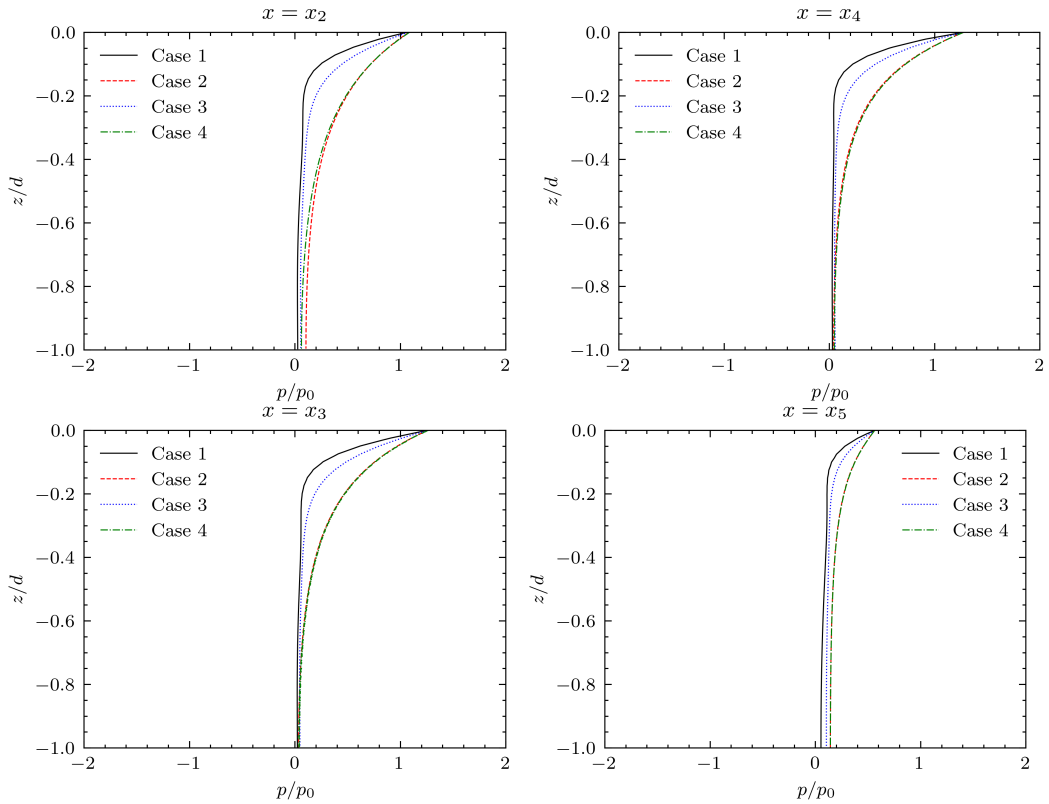

Figure 13. Pore pressure distribution at the wave crest ($t = t_1$) of the spilling breaker for different soil permeability and saturation conditions at various locations.

5.2. Plunging Breaker

Figure 14 compares the computed water surface elevation envelope of the plunging breaker with the experimental data [19], showing that the simulation reasonably captures the wave shoaling and breaking trends. In this case, five locations were also selected to output the free surface elevation and soil stress distribution: x_1 ($x = -2$ m) represents the uniform water-depth region, x_2 ($x = 4$ m) and x_3 ($x = 7.5$ m) are in the wave shoaling

section, and x_4 ($x = 8.5$ m) and x_5 ($x = 11$ m) are in the breaking wave region. Figure 15 shows the computed free-surface elevation at the five locations during the time interval $t = 82T \sim 85T$. The points in the figure represent the output times (t_1 to t_5), which are later used in Figures 17–20. Compared to the spilling breaker case, the longer wavelength of this plunging breaker results in stronger nonlinear effects. As a result, the wave steepness in the constant-depth section is significantly higher, with noticeable high-frequency components. These nonlinear characteristics become even more pronounced after the waves undergo shoaling due to the sloping seabed. Because of the longer wavelength, the breaking point of the plunging breaker occurs later than in the spilling breaker case, and the undertow velocity is also smaller.

Figure 16 displays instantaneous contour plots of fluid velocity and excess pore-water pressure induced by the plunging breaker for soils with different permeabilities. Compared to the results of a spilling breaker (Figure 8), the overall trend is similar despite differences due to wave conditions. As the plunging breaker has a longer wavelength and period with a higher degree of nonlinearity, the wave crest is sharper and the trough more gradual. Consequently, the pore pressure disturbances generated at the wave crest (indicated in red) are spaced further apart and can penetrate deeper into the soil.

Figures 17–20 present the vertical distributions of pore water pressure and stress components before and after breaking for soils with different permeabilities, to investigate the effects of permeability and to compare soil responses under different breaker types. The steepness and asymmetry of the wave profile in the plunging breaker result in significant asymmetry in the cyclic variations of excess pore-water pressure and soil stress, with a deeper range of influence. This difference can be observed in the distribution of σ_{zz} for lower permeability (Case 1) and p for higher permeability (Case 2). By comparing Figures 9 and 17, it can be seen that the asymmetric variation of σ_{zz} in the plunging breaker extends to a greater depth. Similarly, the asymmetric extension of p to deeper depth in the plunging breaker can be observed by comparing Figures 11 and 19. In addition, due to the relatively smaller undertow velocity in the plunging breaker, its influence on soil response in the breaker zone is relatively weaker, but still present. For example, as shown in Figure 20, the periodic variation of p still clearly shifts towards positive values.

Figure 21 illustrates the distribution of excess pore pressure at different locations along the slope for each simulation case at the wave crest ($t = t_1$). The results reveal that the effects of soil permeability and saturation degree are similar to those observed in the previous spilling breaker case. However, due to the longer wavelength of the plunging breaker, excess pore pressure extends deeper into the seabed, highlighting the influence of wave characteristics on pore pressure distribution.

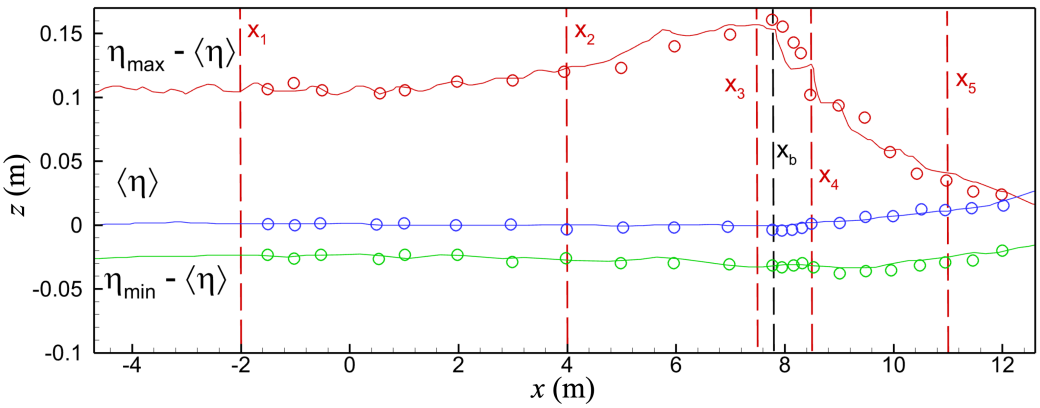

Figure 14. Period-averaged surface elevation envelopes (——) for the plunging breaker simulation, comparing with the experimental measurement [19] (○).

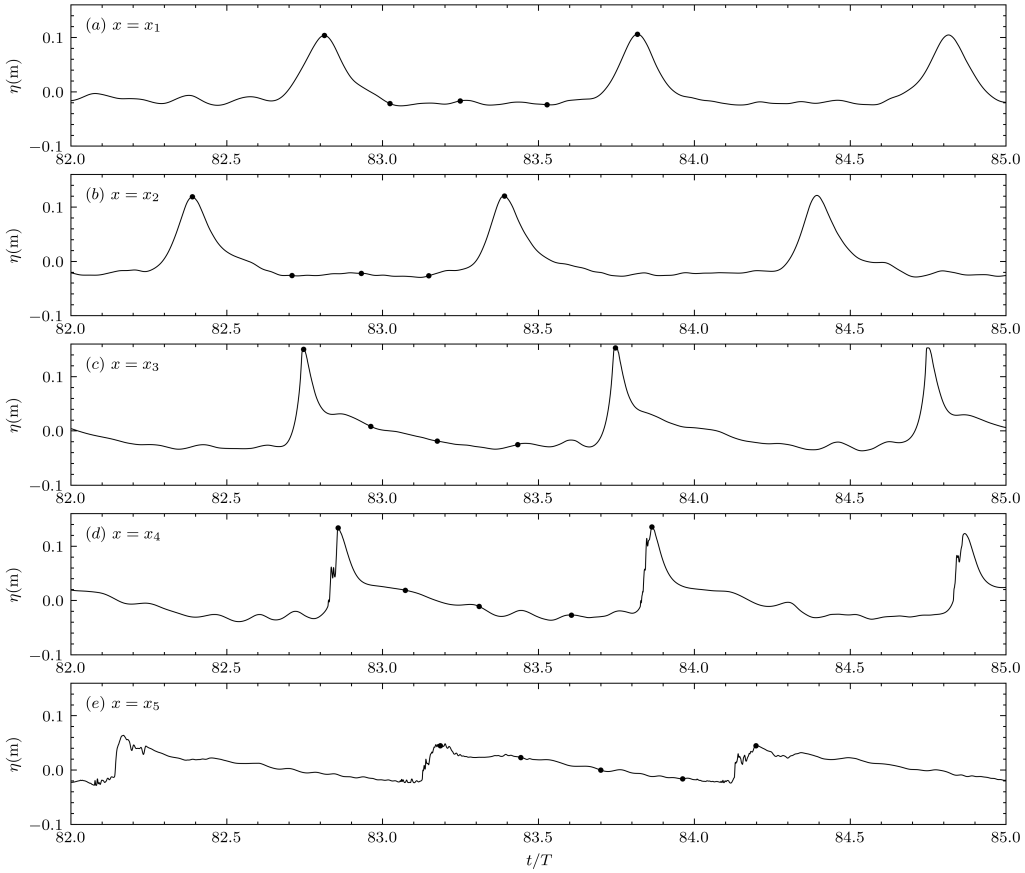

Figure 15. Time variation of free-surface elevation at different locations in the plunging breaker simulation. Points indicate the output times (t_1 to t_5), corresponding to the vertical distribution of pore pressure and soil stresses at each position.

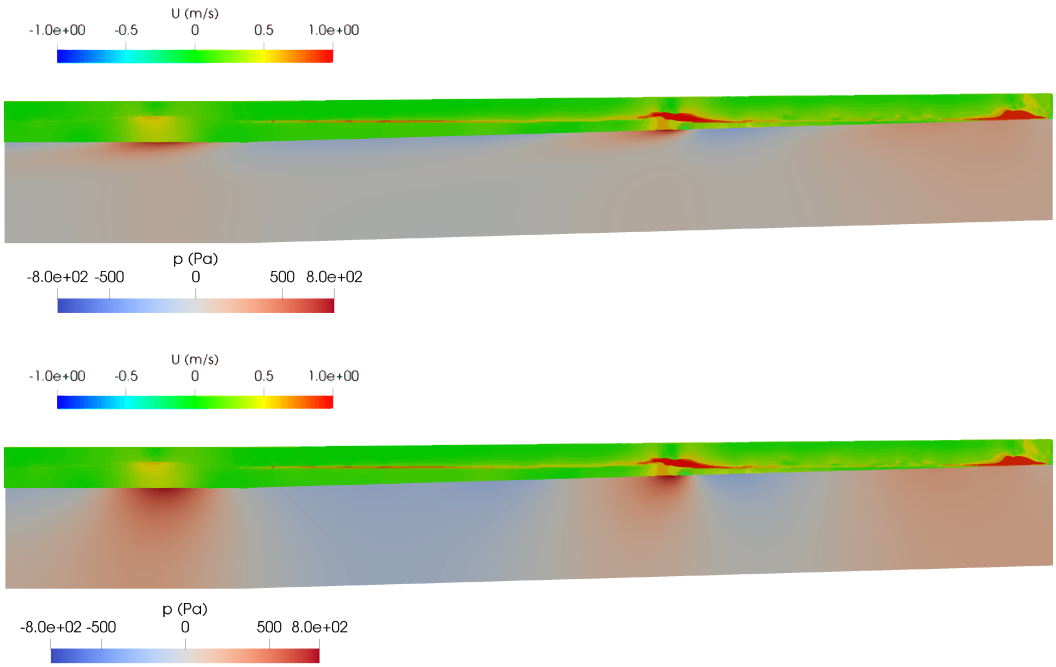

Figure 16. Horizontal fluid velocity and pore pressure contours for Case 1 ($k = 0.0001$ m/s, upper panel) and Case 2 ($k = 0.01$ m/s, lower panel) of plunging breaker simulations.

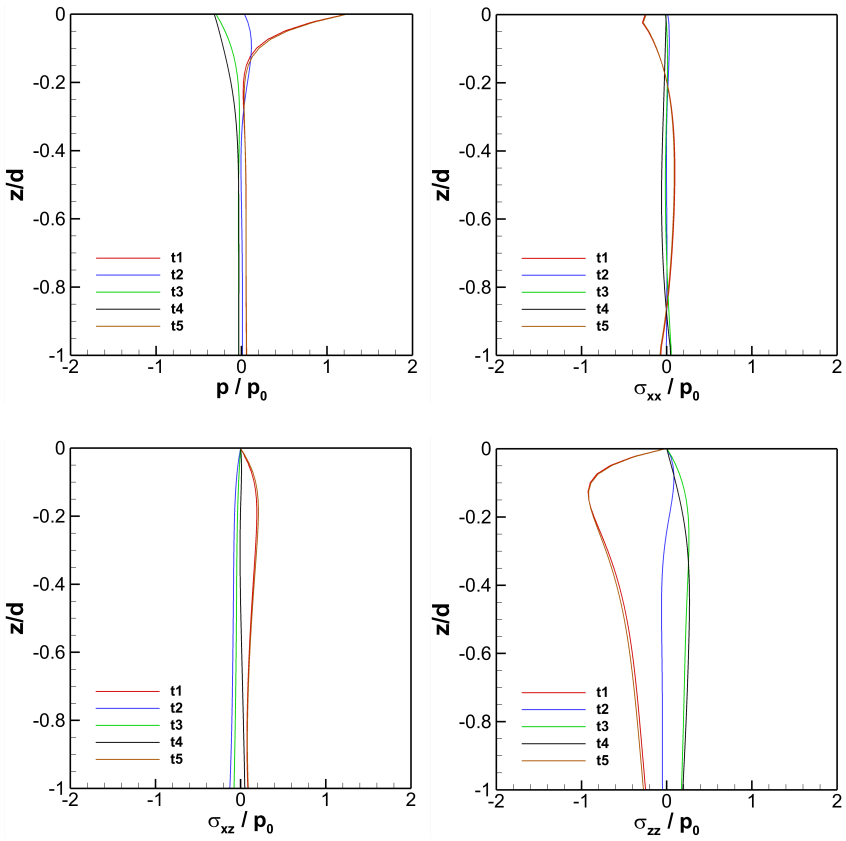

Figure 17. Time variation of pore pressure and soil stresses at location x_3 over one wave period for Case 1 ($k = 0.0001$ m/s) of the plunging breaker simulations.

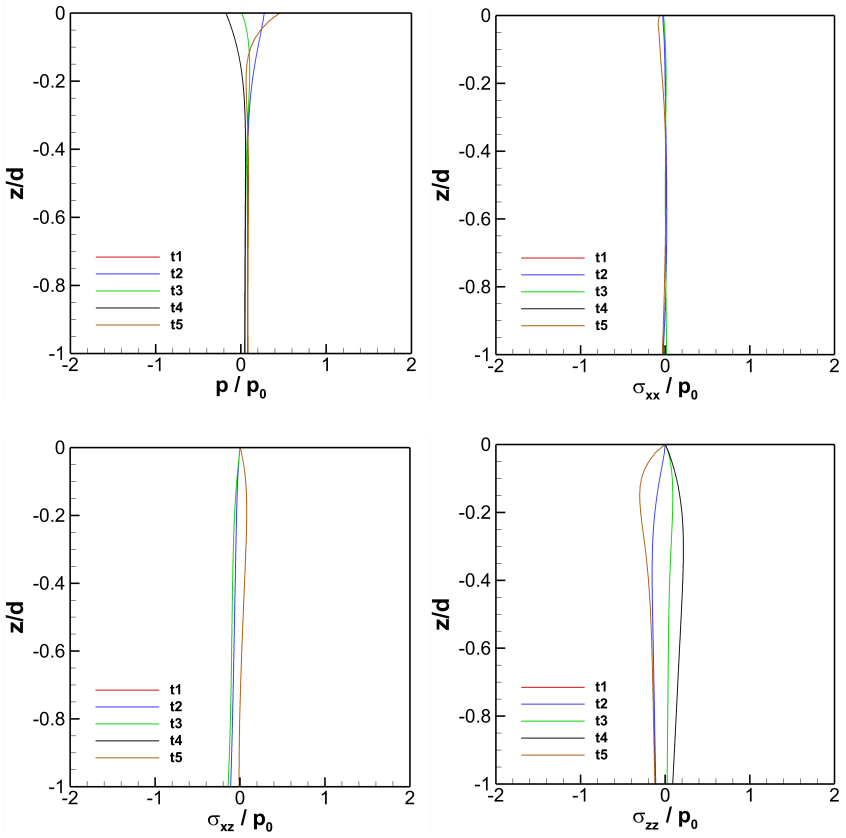

Figure 18. Time variation of pore pressure and soil stresses at location x_5 over one wave period for Case 1 ($k = 0.0001$ m/s) of the plunging breaker simulations.

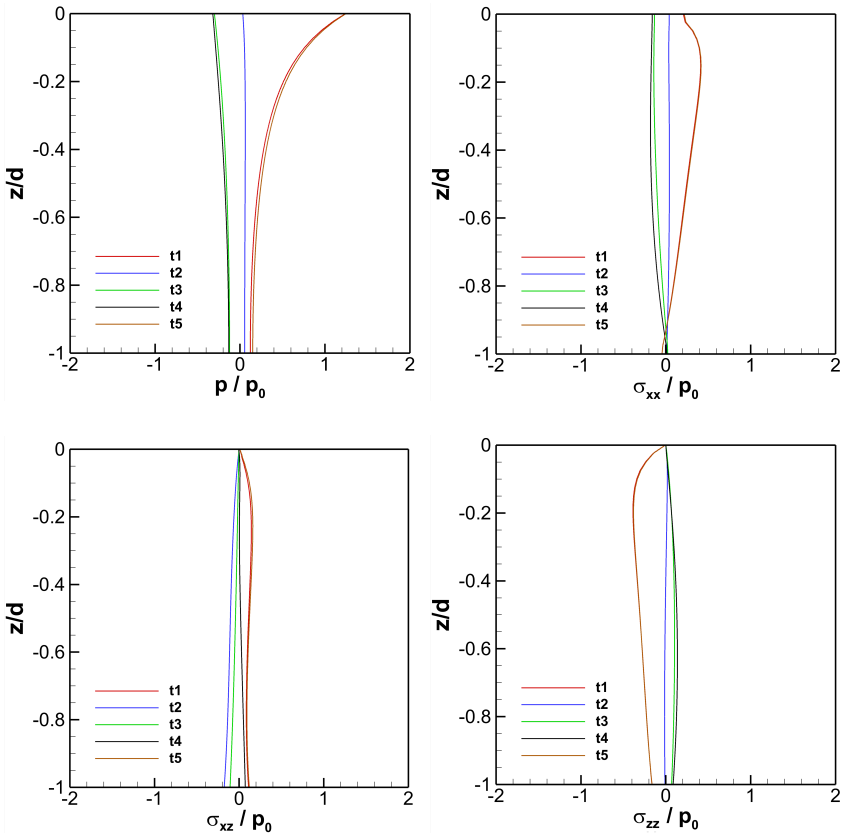

Figure 19. Time variation of pore pressure and soil stresses at location x_3 over one wave period for Case 2 ($k = 0.01$ m/s) of the plunging breaker simulations.

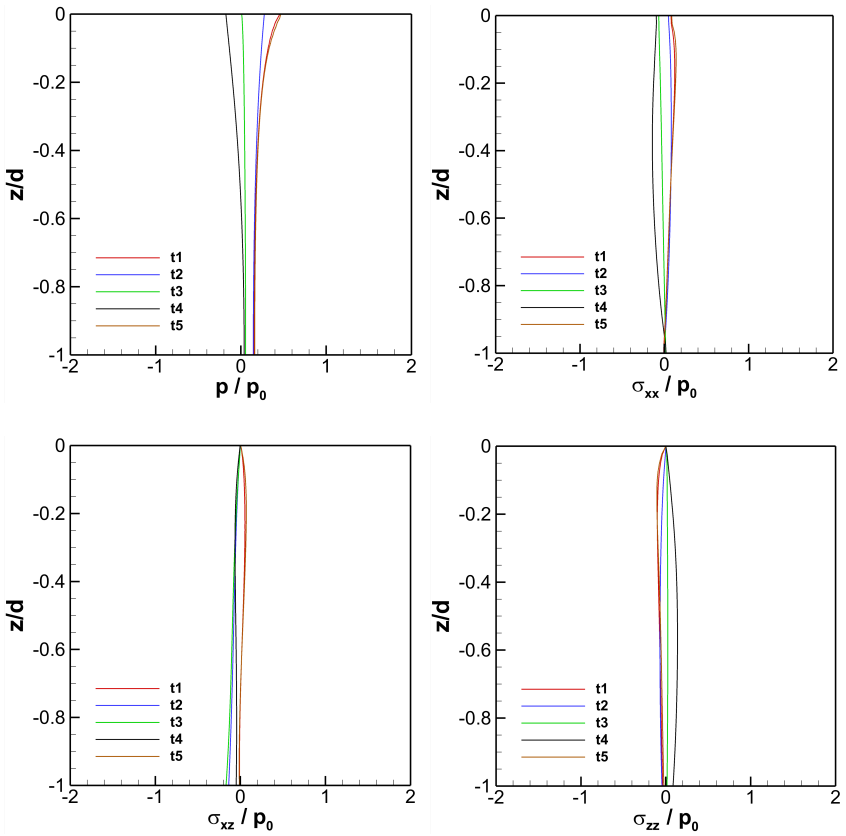

Figure 20. Time variation of pore pressure and soil stresses at location x_5 over one wave period for Case 2 ($k = 0.01$ m/s) of the plunging breaker simulations.

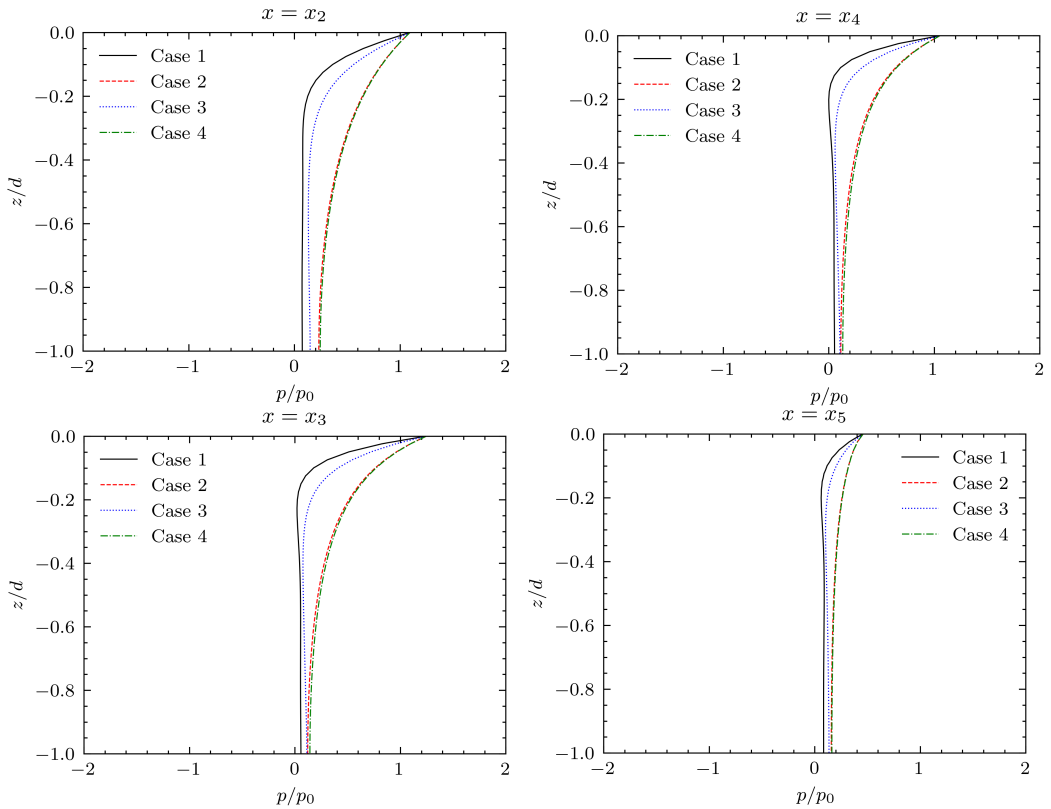

Figure 21. Pore pressure distribution at the wave crest ($t = t_1$) of the plunging breaker for different soil permeability and saturation conditions at various locations.

6. Conclusions

This study utilized the finite volume method (FVM) to develop a two-dimensional numerical model to investigate the seabed soil response induced by wave shoaling and breaking on a sloping bed. The numerical model consists of two components: a wave model and a soil model, connected through a one-way coupling approach.

The wave model simulates turbulent two-phase flow using a stress-ω turbulence model. Comparisons with experimental data demonstrate that the model accurately captures the wave height distribution both before and after breaking. The soil model uses the u-p approximation of Biot's consolidation theory. Numerical experiments indicated that when the ratio of soil depth to wavelength is relatively large, the model yields results more consistent with the quasi-static analytical solution.

Following model validation, we applied the numerical model to simulate and investigate the flow field and soil response for both spilling and plunging breaker cases. The soil conditions primarily focused on the influence of permeability, combined with the saturation degree, to analyze the depth distribution of wave-induced soil responses. The results indicate that wave conditions (wavelength and period) and the resulting breaker type significantly influence the characteristics of the soil response, particularly regarding the periodic oscillation of pore water pressure and stresses, as well as the spatial distribution pattern.

As waves propagate over the sloping seabed, the wave height gradually increases from the flat region, reaching a peak just before breaking, at which point the pore water pressure in the soil is at its maximum. After breaking, the wave height significantly decreases, and the excess pore water pressure also reduces, but due to the influence of the undertow, the overall value shifts in a positive direction.

The spilling breaker type exhibits a more pronounced undertow effect, while the plunging breaker type has a deeper influence on the soil compared to the spilling breaker. When the permeability coefficient is 10^{-2} m/s, the influence of pore water pressure extends deeper, and the vertical transmission of σ_{xx} and σ_{xz} is more pronounced. When the permeability coefficient is 10^{-4} m/s, there is a more significant phase delay in the cyclic oscillations. The degree of saturation in the seabed soil also plays a critical role in its response to wave loading. When the permeability is relatively small, higher saturation degree significantly leads to greater transmission of pore pressure through the soil, extending its influence deeper into the seabed. Although this study varied permeability and saturation to explore their influence, future work may include a broader sensitivity analysis on additional soil parameters such as stiffness and porosity to further evaluate model robustness.

It should be noted that the adopted one-way coupling strategy assumes negligible feedback from the seabed response to the wave field. This assumption is valid in cases where soil deformation and fluid flow within the seabed do not significantly influence the hydrodynamic processes, such as in non-liquefied soils with limited deformation. However, for conditions involving severe seabed softening, sediment transport, or potential liquefaction, two-way coupling may be required to capture the full interaction [33]. Such scenarios are beyond the scope of the present study but represent an important direction for future work. In addition, direct validation of seabed pore pressure or stress under breaking waves could not be performed due to the limited availability of such experimental or field data. Future studies incorporating measurements of seabed response under breaking conditions would be valuable for further validation and model development.

In conclusion, the findings of this study emphasize the importance of considering both wave dynamics and seabed properties in understanding coastal processes. The numerical model provides a useful tool for investigating the complex interactions between breaking waves and seabed soils and can help inform the design of coastal and offshore structures, ensuring their stability under dynamic wave loading conditions.

Author Contributions: Conceptualization, M.-Y.L. and T.-H.C.; methodology, M.-Y.L.; software, M.-Y.L. and Y.-X.L.; validation, Y.-X.L.; formal analysis, M.-Y.L.; investigation, M.-Y.L. and Y.-X.L.; resources, M.-Y.L. and T.-H.C.; data curation, M.-Y.L.; writing—original draft preparation, M.-Y.L. and Y.-X.L.; writing—review and editing, M.-Y.L.; visualization, M.-Y.L. and Y.-X.L.; supervision, T.-H.C.; project administration, M.-Y.L.; funding acquisition, M.-Y.L. All authors have read and agreed to the published version of the manuscript.

Funding: This research was funded by the National Science and Technology Council of Taiwan, R.O.C. (MOST 111-2221-E-033-021) and the John Su Foundation.

Data Availability Statement: The data used in this study are available upon reasonable request from the authors.

Acknowledgments: The authors sincerely thank the National Science and Technology Council of Taiwan, R.O.C., and the John Su Foundation for their financial support. Appreciation is also extended to the anonymous reviewers for their valuable comments and constructive suggestions, which have greatly improved the quality of this manuscript.

Conflicts of Interest: The authors declare no conflicts of interest. The funders had no role in the design of the study; in the collection, analyses, or interpretation of data; in the writing of the manuscript; or in the decision to publish the results.

References

1. Madsen, O.S. Wave-induced pore pressures and effective stresses in a porous bed. *Géotechnique* **1978**, *28*, 377–393. [CrossRef]
2. Yamamoto, T.; Koning, H.L.; Sellmeijer, H.; Hijum, E.V. On the response of a poro-elastic bed to water waves. *J. Fluid Mech.* **1978**, *87*, 193–206. [CrossRef]
3. Biot, M.A. General theory of three-dimensional consolidation. *J. Appl. Phys.* **1941**, *12*, 155–164. [CrossRef]
4. Zienkiewicz, O.C.; Chang, C.T.; Bettess, P. Drained, undrained, consolidating and dynamic behaviour assumptions in soils. *Géotechnique* **1980**, *30*, 385–395. [CrossRef]
5. Mei, C.C.; Foda, M.A. Wave-induced responses in a fluid-filled poro-elastic solid with a free surface—A boundary layer theory. *Geophys. J. Int.* **1981**, *66*, 597–631. [CrossRef]
6. Okusa, S. Wave-induced stresses in unsaturated submarine sediments. *Géotechnique* **1985**, *35*, 517–532. [CrossRef]
7. Hsu, J.R.C.; Jeng, D.S.; Tsai, C.P. Short-crested wave-induced soil response in a porous seabed of infinite thickness. *Int. J. Numer. Anal. Methods Geomech.* **1993**, *17*, 553–576. [CrossRef]
8. Jeng, D.S.; Cha, D. Effects of dynamic soil behavior and wave non-linearity on the wave-induced pore pressure and effective stresses in porous seabed. *Ocean Eng.* **2003**, *30*, 2065–2089. [CrossRef]
9. Jeng, D.S. Wave-induced sea floor dynamics. *Appl. Mech. Rev.* **2003**, *56*, 407–423. [CrossRef]
10. Ulker, M.B.C.; Rahman, M.S.; Jeng, D.S. Wave-induced response of seabed: Various formulations and their applicability. *Appl. Ocean Res.* **2009**, *31*, 12–24. [CrossRef]
11. Arcos, E.; Bautista, E.; Méndez, F. Dynamic response of a poro-elastic soil to the action of long water waves: Determination of the maximum liquefaction depth as an eigenvalue problem. *Appl. Ocean Res.* **2017**, *67*, 213–224. [CrossRef]
12. Wang, G.; Chen, S.; Liu, Q.; Zhang, Y. Wave-induced dynamic response in a poroelastic seabed. *J. Geotech. Geoenviron. Eng.* **2018**, *144*, 06018008. [CrossRef]
13. Dalrymple, R.A. Prediction of storm/normal beach profiles. *J. Waterw. Port Coast. Ocean Eng.* **1992**, *118*, 193–200. [CrossRef]
14. Svendsen, I.A. Analysis of surf zone turbulence. *J. Geophys. Res. Oceans* **1987**, *92*, 5115–5124. [CrossRef]
15. Dean, R.G. Heuristic models of sand transport in the surf zone. In Proceedings of the First Australian Conference on Coastal Engineering, 1973: Engineering Dynamics of the Coastal Zone, Sydney, Australia, 14–17 May 1973; pp. 215–221.
16. Mahmoudof, S.M.; Siadatmousavi, S.M.; Takami, M.L. Numerical study of cross-shore variations of bound super-harmonics over a single sandbar system. *Ocean Eng.* **2022**, *266*, 112695. [CrossRef]
17. Gao, J.; Shi, H.; Zang, J.; Liu, Y. Mechanism analysis on the mitigation of harbor resonance by periodic undulating topography. *Ocean Eng.* **2023**, *281*, 114923. [CrossRef]
18. Gao, J.; Hou, L.; Liu, Y.; Shi, H. Influences of bragg reflection on harbor resonance triggered by irregular wave groups. *Ocean Eng.* **2024**, *305*, 117941. [CrossRef]
19. Ting, F.C.K.; Kirby, J.T. Observation of undertow and turbulence in a laboratory surf zone. *Coast. Eng.* **1994**, *24*, 51–80. [CrossRef]
20. Lin, P.; Liu, P.L.F. A numerical study of breaking waves in the surf zone. *J. Fluid Mech.* **1998**, *359*, 239–264. [CrossRef]
21. Dong, G.; Chen, H.; Ma, Y. Parameterization of nonlinear shallow water waves over sloping bottoms. *Coast. Eng.* **2014**, *94*, 23–32. [CrossRef]
22. Ma, Y.; Chen, H.; Ma, X.; Dong, G. A numerical investigation on nonlinear transformation of obliquely incident random waves on plane sloping bottoms. *Coast. Eng.* **2017**, *130*, 65–84. [CrossRef]
23. Zhang, J.; Benoit, M. Wave–bottom interaction and extreme wave statistics due to shoaling and de-shoaling of irregular long-crested wave trains over steep seabed changes. *J. Fluid Mech.* **2021**, *912*, A28. [CrossRef]
24. Larsen, B.E.; Fuhrman, D.R. On the over-production of turbulence beneath surface waves in Reynolds-averaged Navier–Stokes models. *J. Fluid Mech.* **2018**, *853*, 419–460. [CrossRef]
25. Li, Y.; Larsen, B.E.; Fuhrman, D.R. Reynolds stress turbulence modelling of surf zone breaking waves. *J. Fluid Mech.* **2022**, *937*, A7. [CrossRef]
26. Rafiei, A.; Rahman, M.; Gabr, M. Coupled analysis for response and instability of sloping seabed under wave action. *Appl. Ocean Res.* **2019**, *88*, 99–110. [CrossRef]
27. Wilcox, D.C. *Turbulence Modeling for CFD*, 3rd ed.; DCW Industries: La Cãnada, CA, USA, 2006.
28. Li, Y.; Ong, M.C.; Tang, T. A numerical toolbox for wave-induced seabed response analysis around marine structures in the OpenFOAM® framework. *Ocean Eng.* **2020**, *195*, 106678. [CrossRef]
29. Hirt, C.; Nichols, B. Volume of fluid (VOF) method for the dynamics of free boundaries. *J. Comput. Phys.* **1981**, *39*, 201–225. [CrossRef]
30. Berberović, E.; Van Hinsberg, N.P.; Jakirlić, S.; Roisman, I.V.; Tropea, C. Drop impact onto a liquid layer of finite thickness: Dynamics of the cavity evolution. *Phys. Rev. E* **2009**, *79*, 036306. [CrossRef]
31. Jacobsen, N.G.; Fuhrman, D.R.; Fredsøe, J. A wave generation toolbox for the open-source CFD library: OpenFoam®. *Int. J. Numer. Methods Fluids* **2011**, *70*, 1073–1088. [CrossRef]

32. Hsu, J.R.C.; Jeng, D.S. Wave-induced soil response in an unsaturated anisotropic seabed of finite thickness. *Int. J. Numer. Anal. Methods Geomech.* **1994**, *18*, 785–807. [CrossRef]
33. Zhai, H.; Jeng, D.S. Two-way coupling model for wave-induced oscillatory soil response around marine structures. *Ocean Eng.* **2022**, *249*, 110791. [CrossRef]

Disclaimer/Publisher's Note: The statements, opinions and data contained in all publications are solely those of the individual author(s) and contributor(s) and not of MDPI and/or the editor(s). MDPI and/or the editor(s) disclaim responsibility for any injury to people or property resulting from any ideas, methods, instructions or products referred to in the content.